

# IRC +10 216 revisited II: the circumstellar CO shell <sup>\*</sup>

M.A.T. Groenewegen<sup>1</sup>, W.E.C.J. van der Veen<sup>2</sup>, and H.E. Matthews<sup>3</sup>

<sup>1</sup> Max-Planck-Institut für Astrophysik, Karl-Schwarzschild-Straße 1, D-85740 Garching, Germany

<sup>2</sup> Department of Astronomy, Columbia University, 538 West 120th Street, New York, NY 10027, U.S.A.

<sup>3</sup> Joint Astronomy Centre, 660 N. A'ohōkū Place, University Park, Hilo, Hawaii 96720, U.S.A., and Herzberg Institute of Astrophysics, NRC of Canada, 5071 W. Saanich Road, Victoria, B.C. V8X 4M6, Canada

received 29 September 1997, accepted 30 June 1998

**Abstract.** <sup>12</sup>CO and <sup>13</sup>CO J = 6-5 observations of IRC +10 216 with the JCMT are presented. A spherically symmetric radiative transfer code is used to model these and other CO observations of the carbon star IRC +10 216/CW Leo. Compared to previously published model calculations a much larger set of observational data is used as constraints; on-source <sup>12</sup>CO and <sup>13</sup>CO J = 1-0 up to J = 6-5 and mapping data taken with various telescopes, most of which are obtained from the literature.

The gas temperature in the envelope is calculated taking into account heating and cooling. The heating by dust-gas collisions and various other parameters (such as luminosity over distance squared) are constrained from our previous modeling of the circumstellar dust shell. Photoelectric heating is taken into account.

A grid of models is calculated with the following parameters: luminosity (in the range 10 000 – 30 000, in steps of 5 000 L<sub>⊙</sub>), mass loss rate, dust-to-gas ratio, dust opacity and CO abundance. For each of the considered luminosities a good fit to the on-source data can be obtained. A comparison with CO J = 1-0 data obtained from the literature points towards a preferred luminosity of 10-15 000 L<sub>⊙</sub>.

Notwithstanding the overall good agreement, there remain discrepancies. The different observed <sup>12</sup>CO J = 3-2 observations appear to be always larger than the model predictions. The observed <sup>13</sup>CO J = 6-5 is almost flat-topped, while the model gives a slight double-peaked profile. There is a large discrepancy with the single existing <sup>12</sup>CO J = 7-6 observation.

The best fitting models (for each of the considered luminosities) cannot accommodate the more extended emis-

sion seen in the mapping data. This is not due to an underestimate of the photoelectric effect. To fit the data for radial offsets >50'' the mass loss rate must be a factor of 5 higher in the outer envelope. Because the various sets of data for offsets ≳150'' are not consistent with each other it is unclear if the enhancement in the mass loss rate extends beyond that radius.

Visibility curves are calculated for comparison with future interferometric observations. These appear to be insensitive to luminosity and mass loss variations but should be good tracers of the geometry of the CO shell.

A comparison is made between the mass loss rates and dust-to-gas ratios derived from the CO modelling and those derived from our previous dust modelling. To do this we make use of the relation  $\dot{M} v_{\infty} = \tau_{\text{F}} \frac{L}{c} \left(1 - \frac{1}{\text{F}}\right)$ , which is valid for radiation pressure driven outflows. The best agreement is obtained for the model with 15 000 L<sub>⊙</sub>. This agrees well with the luminosity range 7 700-12 500 L<sub>⊙</sub> based on the period-luminosity relation for carbon miras.

In summary, we conclude that the likely luminosity of IRC +10 216 is between 10 000 and 15 000 L<sub>⊙</sub> and that its distance is between 110 and 135 pc. The present-day mass loss rate is  $(1.5 \pm 0.3) \times 10^{-5} \text{ M}_{\odot} \text{ yr}^{-1}$  and the gas-to-dust ratio is  $700 \pm 100$ . The dust opacity at 60 μm is found to be of order of 250 cm<sup>2</sup>gr<sup>-1</sup>. The CO abundance is  $1.1 \times 10^{-3}$  relative to H<sub>2</sub>.

**Key words:** circumstellar matter – stars: individual: IRC +10 216 – mass loss – AGB, post-AGB – radio lines: stars

Send offprint requests to: Martin Groenewegen (groen@mpa-garching.mpg.de)

\* The James Clerk Maxwell Telescope is operated by the Joint Astronomy Centre on behalf of the Particle Physics and Astronomy Research Council of the United Kingdom, the Netherlands Organization for Scientific Research, and the National Research Council of Canada.

## 1. Introduction

IRC +10 216 (= AFGL 1381 = CW Leo) is the best-studied carbon star, because it is intrinsically bright and nearby. One aspect of study has traditionally been the properties of the circumstellar shell: e.g., what is the mass loss rate, has the mass loss rate changed with time, what

kind of chemistry takes place, what is the geometry of the shell?

In two recent papers we have made an extensive study of the circumstellar dust shell of IRC +10 216 (Groenewegen 1996, 1997, hereafter G97). A much larger set of observational constraints was used than in any previous study. This allowed the derivation of the present-day dust mass loss rate, the ratio between the luminosity at maximum light divided by the distance squared, the dominant grain size, the effective temperature and the inner dust radius.

In another paper we have mapped the 1.3 mm continuum emission around the star (Groenewegen et al. 1997). It was detected out to  $50''$  at a noise level of  $3\sigma$  or better. There is evidence for phases of enhanced mass loss, but a quantitative analysis is hampered by the significant contribution of molecular lines to the continuum emission, and the uncertainty in the radial distribution of that contribution.

Another way to study the circumstellar shell is by observing the gas component. A good tracer of the ( $\text{H}_2$ ) gas is the CO molecule, and numerous CO observations exist of IRC +10 216 (see the catalog of Loup et al. (1993) for a compilation). A fair number of detailed models have been proposed to explain various CO observations. The pioneering work was done by Kwan & Hill (1977). For an assumed distance of 200 pc they deduced a mass loss rate of  $2 \times 10^{-5} M_{\odot} \text{ yr}^{-1}$ , a CO abundance relative to  $\text{H}_2$  of about  $8 \times 10^{-4}$  (both uncertain to a factor of 2), and a  $\text{CO}/^{13}\text{CO}$  isotope ratio of  $35 \pm 7$ . In a second paper Kwan & Linke (1982) deduced a mass loss rate of  $4 \times 10^{-5} M_{\odot} \text{ yr}^{-1}$  for a distance of 200 pc and a CO abundance of  $6 \times 10^{-4}$ . Sahai (1987) finds, based on the modeling of high-J lines, that the temperature in the inner region is much larger than that predicted by the Kwan & Linke model, and that the mass loss rate in the inner  $6''$  region is  $3.2 \times 10^{-5} M_{\odot} \text{ yr}^{-1}$  and 50% higher in the extended envelope, assuming a distance of 300 pc and a CO abundance of  $8 \times 10^{-4}$ . Truong-Bach et al. (1991) also find evidence for a hot inner core: a mass loss rate of  $2.5 \times 10^{-5} M_{\odot} \text{ yr}^{-1}$  in the inner  $4.2''$  and a mass loss rate of  $4 \times 10^{-5} M_{\odot} \text{ yr}^{-1}$  in the outer region (for a distance of 200 pc). Kastner (1992) found a best fit to some CO data for a distance of 150 pc and a mass loss rate of  $2 \times 10^{-5} M_{\odot} \text{ yr}^{-1}$ . In a recent paper, Crosas & Menten (1997) also presented J = 6-5  $^{12}\text{CO}$  and  $^{13}\text{CO}$  data, and combined those with other data from the literature, and modelled the data. In this respect the philosophy behind that paper is similar to ours. The major differences with that paper are that the effective absorption coefficient is taken into account in a consistent way (see below and Sect. 7.2) and that the parameter space is scanned consistently no a-priori fixing any parameter. In Crosas & Menten, the dust-to-gas ratio is *fixed* at a value of 0.01. They find a good fit using a distance of 150 pc, a mass loss rate of  $3.25 \times 10^{-5} M_{\odot} \text{ yr}^{-1}$ , a CO abundance of  $6 \times 10^{-4}$ , and a dust-gas momentum transfer rate  $Q$  of 0.025 for the inner region ( $r \leq 10^{16}$  cm),

and 0.018 for the outer region. They conclude there is no need for a hot inner core.

In all the model calculations mentioned above the effective absorption coefficient  $Q$  is assumed to be a free parameter.  $Q$  describes the momentum transfer efficiency between the gas and the dust. However, we claim, and this is a key point in this paper, that effective absorption coefficient  $Q$  is not a free parameter but is related to the properties of the dust. This had been realised before but it requires the simultaneous fitting of the spectral energy distribution (SED) and the CO data in order to estimate  $Q$  in a self-consistent way. This approach was taken in the fitting of two OH/IR stars in Groenewegen (1994b) and is proposed here for IRC +10 216.

The outline of the paper is as follows. In Sects. 2 and 3 the model is briefly described. In Sect. 4 the  $^{12}\text{CO}$  and  $^{13}\text{CO}$  J = 6-5 observations as well as the other CO data to which the models are compared are presented. In Sect. 5 the results of the model calculations are described. So-called visibility curves, to be compared with future interferometric observations, are presented in Sect. 6. The paper ends with discussion and conclusions in Sect. 7.

## 2. The model

The calculations are performed with the molecular line emission radiative transfer model of Groenewegen (1994a; G94). This model is an improvement over and extension of the code by Morris et al. (1985) through the inclusion of a self-consistent determination of the gas temperature. The model was previously applied to two OH/IR stars at known distances (Groenewegen 1994b).

The model is fully described in G94 and only some essential details are repeated here. The model assumes spherical symmetry and that the Sobolev approximation is valid to calculate the radiative transfer (this presumes that the local linewidth is much smaller than the expansion velocity). The line profiles are calculated without the Sobolev approximation using a ray-tracing method instead, assuming, in the present paper, a thermal velocity of  $0.5 \text{ km s}^{-1}$ . The CO, respectively  $^{13}\text{CO}$  or HCN, molecules are excited by: (1) collisions with  $\text{H}_2$  and He molecules, (2) interaction with the 2.8 K background radiation, and (3) infrared radiation from a central blackbody of temperature  $T_{\text{BB}}$  and radius  $R_{\text{BB}}$  which leads to pumping from the  $v = 0$  into the  $v = 1$  vibrational state.

The heating rate by the photoelectric effect is discussed in G94. The heating rate per hydrogen molecule is not simply a constant as is often assumed, but the grain charge parameter is calculated for each radius and optical depth effects are taken into account. The photoelectric heating rate scales as  $(G_0(Y/0.1))$ , with  $G_0$  the UV flux of the diffuse interstellar medium, and  $Y$  the yield of dust grains.  $G_0 = 1$  and  $Y = 0.1$  are used unless otherwise noted.

**Table 1.** CO data used as constraints

Molecule	Transition	Reference	Telescope	Beam width FWHM(")	Remark
$^{12}\text{CO}$	1-0	Groenewegen et al. (1996)	IRAM	21.0	primary constraint
		Truong-Bach et al. (1991)	IRAM	21.0	map
		Groenewegen & Ludwig (1998)	IRAM	21.0	map
		Knapp & Morris (1985)	BTL	100	
		Huggins et al. (1988)	NRAO	50	map
		Olofsson et al. (1993)	SEST	45	
	2-1	Groenewegen et al. (1996)	IRAM	12.5	primary constraint
		Truong-Bach et al. (1991)	IRAM	12.5	map
		Groenewegen & Ludwig (1998)	IRAM	12.5	map
	3-2	Huggins et al. (1988)	NRAO	31	map
		Olofsson et al. (1993)	SEST	23	
		Groenewegen et al. (1996)	JCMT	14.3	primary constraint
	4-3	Williams & White (1992)	JCMT	15	
Wang et al. (1994)		CSO	21.4		
6-5	Williams & White (1992)	JCMT	11.0	primary constraint	
7-6	this paper	JCMT	55% in 7.0" + 45% in 18" beam	primary constraint	
$^{13}\text{CO}$	1-0	Wattenbach et al. (1988)	UH 2.2m	45	
		Groenewegen et al. (1996)	IRAM	21.0	primary constraint
	2-1	Knapp & Chang (1985)	BTL	105	
		Groenewegen et al. (1996)	IRAM	12.5	primary constraint
	3-2	Groenewegen et al. (1996)	JCMT	14.3	primary constraint
		Williams & White (1992)	JCMT	15	
		Wang et al. (1994)	CSO	20.3	
	6-5	this paper	JCMT	55% in 7.0" + 45% in 18" beam	primary constraint

The heating rate per unit volume caused by dust-gas collisions is (see G94 for details):

$$H_{\text{dg}} \sim n(\text{H}_2)^2 \frac{\Psi (1 + 4 f_{\text{He}})^2}{a \rho_d} \left( \frac{L Q v(r)}{\dot{M}} \right)^{3/2} \quad (1)$$

and the drift velocity in  $\text{km s}^{-1}$  given by:

$$v_{\text{dr}} = 1.4293 \times 10^{-4} \left( \frac{L Q v(r)}{\dot{M}} \right)^{0.5} \quad (2)$$

where  $\rho_d$  is the dust grain density,  $a$  the grain size,  $L$  the stellar luminosity in solar units,  $\dot{M}$  the mass loss rate in  $M_{\odot}/\text{yr}$ ,  $Q$  the effective absorption coefficient (defined below in Eq. 4),  $v(r)$  the gas velocity in  $\text{km s}^{-1}$ ,  $f_{\text{He}}$  the number ratio of helium to hydrogen (a value of 0.1 is assumed) and  $\Psi$  the dust-to-gas ratio.

The cooling rate is determined by molecular line cooling of  $^{12}\text{CO}$ ,  $^{13}\text{CO}$ , HCN,  $\text{H}_2$  and adiabatic cooling. The  $\text{H}_2$  cooling rate is treated in an approximate way but is not very important (G94). The cooling rate due to  $^{12}\text{CO}$ ,  $^{13}\text{CO}$  and HCN is calculated from the molecular excitation code in an iterative process. For a given temperature structure the level populations are calculated, which allows the molecular cooling to be determined, and finally a new temperature structure is derived by solving the energy balance equation (see G94).

### 2.1. How does dust affect the molecular excitation model?

As mentioned before dust grain-gas collisions is the most important heating mechanism and therefore the properties of the dust (size, opacity, dust-to-gas ratio) influence the gas temperature and hence the resulting CO line profiles.

In G97 the spectral energy distribution (SED) and visibility curves of IRC +10 216 were modelled using a dust radiative transfer (DRT) model and constraints were set to the dust properties. Table 2 lists for an assumed luminosity, the derived mass loss rate and distance.

**Table 2.** Default parameters

Luminosity ( $L_{\odot}$ )	Distance <sup>(1)</sup> (pc)	$\dot{M}_{\text{def}}$ <sup>(1)</sup> $10^{-5} M_{\odot} \text{ yr}^{-1}$
10 000	110	1.80
15 000	135	2.20
20 000	156	2.54
25 000	174	2.84
30 000	191	3.11

<sup>(1)</sup>Parameters that follow from the dust modeling in G97. The mass loss rate is based on  $\Psi = 0.005$ ,  $\kappa_{60} = 68 \text{ cm}^2 \text{ gr}^{-1}$  and a dust expansion velocity of  $17.5 \text{ km s}^{-1}$ .

**Table 3.** Grid of models ran

	$\Psi$	$\Psi/1.2$	$\Psi/1.25$	$\Psi/1.5$	$\Psi/1.67$	$\Psi/1.8$	$\Psi/2$	$\Psi/3$	$\Psi/4$	$\Psi/5$
L = 10 000 L <sub>⊙</sub>										
$\dot{M}_{\text{def}} \times 1.0$	9	-	-	-	-	-	10	10	-	9
$\dot{M}_{\text{def}} / 1.2$	-	-	-	-	-	-	-	10	<b>11</b>	-
$\dot{M}_{\text{def}} / 1.4$	-	-	-	-	-	-	-	13	-	-
$\dot{M}_{\text{def}} / 1.8$	-	-	-	-	-	-	16	-	-	-
L = 15 000 L <sub>⊙</sub>										
$\dot{M}_{\text{def}} \times 1.2$	-	-	-	-	-	-	-	-	-	8
$\dot{M}_{\text{def}} \times 1.0$	9	-	-	-	-	-	9	9	9	-
$\dot{M}_{\text{def}} / 1.2$	10	-	-	-	-	-	10	<b>11</b>	-	-
$\dot{M}_{\text{def}} / 1.4$	12	-	-	-	-	-	12	-	-	-
$\dot{M}_{\text{def}} / 1.6$	14	-	14	-	-	-	-	-	-	-
L = 20 000 L <sub>⊙</sub>										
$\dot{M}_{\text{def}} \times 1.2$	-	-	-	-	-	-	-	-	-	8
$\dot{M}_{\text{def}} \times 1.0$	9	-	-	-	-	-	10	9	-	-
$\dot{M}_{\text{def}} / 1.2$	-	-	-	-	-	-	-	<b>12</b>	-	-
$\dot{M}_{\text{def}} / 1.4$	-	-	-	-	14	-	-	-	-	-
L = 25 000 L <sub>⊙</sub>										
$\dot{M}_{\text{def}} \times 1.4$	-	-	-	-	-	-	7	7	7	-
$\dot{M}_{\text{def}} \times 1.2$	-	8	-	-	-	-	8	-	8	<b>8</b>
$\dot{M}_{\text{def}} \times 1.0$	9	-	-	-	-	-	10	9	-	-
$\dot{M}_{\text{def}} / 1.2$	10	-	-	-	-	-	10	11	-	-
$\dot{M}_{\text{def}} / 1.4$	12	-	-	-	-	13	12	-	-	-
$\dot{M}_{\text{def}} / 1.6$	15	-	15	-	-	-	12	-	-	-
$\dot{M}_{\text{def}} / 1.8$	17	-	-	-	-	-	-	-	-	-
L = 30 000 L <sub>⊙</sub>										
$\dot{M}_{\text{def}} \times 1.2$	-	8	-	-	-	-	-	-	-	-
$\dot{M}_{\text{def}} \times 1.0$	10	-	-	-	-	-	10	<b>10</b>	-	-
$\dot{M}_{\text{def}} / 1.2$	10	-	-	-	-	-	11	-	-	-
$\dot{M}_{\text{def}} / 1.4$	11	-	-	12	-	-	-	-	-	-

For every luminosity the combinations of models that have been calculated are indicated. The corresponding absolute dust opacity follows from Eq. (3). The default mass loss rate and the distance are different for each luminosity; see Table 2. The entry in the table is the best fitting CO abundance in units of  $10^{-4}$ . Bold-faced numbers indicate best-fitting models discussed in Sect. 5.

The shape of the calculated SED is determined completely by the input spectrum of the underlying star, the inner dust radius (or equivalently, the temperature of the dust at the inner radius,  $T_c$ ), and the optical depth. The optical depth is given by:

$$\tau_\lambda = \int_{r_{\text{inner}}}^{r_{\text{outer}}} \pi a^2 Q_\lambda n_d(r) dr$$

$$\sim \frac{\dot{M} \Psi Q_\lambda / a}{R_\star v_\infty \rho_d r_c} \int_1^{r_{\text{max}}} \frac{R(x)}{x^2 w(x)} dx \quad (3)$$

where  $x = r/r_c$ ,  $\dot{M}(r) = \dot{M} R(x)$  and  $v(r) = v_\infty w(x)$ . The normalized mass loss rate profile  $R(x)$  and the normalized velocity law  $w(x)$  should obey  $R(1) = 1$  and  $w(\infty) = 1$ , respectively. In the case of a constant mass loss rate and a constant velocity, the integral in Eq. (3) is essentially unity since  $r_{\text{max}}$  is always much larger than 1. The symbols and units in Eq. (3) are: the (present-day) mass loss rate  $\dot{M}$  in  $M_\odot \text{ yr}^{-1}$ ,  $\Psi$  the dust-to-gas mass ratio (assumed constant with radius),  $Q_\lambda$  the extinction coefficient,  $a$  the grain size in cm (the model assumes a single grain

size),  $R_*$  the stellar radius in solar radii,  $v_\infty$  the terminal velocity of the dust in  $\text{km s}^{-1}$ ,  $\rho_d$  the dust grain specific density in  $\text{g cm}^{-3}$ ,  $r_c$  the inner dust radius in units of stellar radii and  $r_{\text{max}}$  the outer radius in units of  $r_c$ . The mass loss rates derived in G97 are based on an assumed dust velocity of  $17.5 \text{ km s}^{-1}$ , an absolute opacity at  $60 \mu\text{m}$  of  $68 \text{ cm}^2 \text{g}^{-1}$  and a dust-to-gas ratio of 0.005.

The relation between the wavelength dependent absorption coefficient  $Q_\lambda$  in Eq. (3) and the effective absorption coefficient  $Q$  in Eq. (1) is:

$$Q = \frac{\int F_\lambda Q_\lambda d\lambda}{\int F_\lambda d\lambda} \quad (4)$$

where  $F_\lambda$  is the emerging flux from the central star and the dust shell at infinity. In principle  $Q$  depends on the radius since  $F_\lambda$  is continuously changed by the dust emission but this is only important near the inner radius where the dust temperature changes rapidly (see Habing et al. 1994). The molecular transitions under discussion here originate from several tens to hundreds of stellar radii where  $F_\lambda$  is essentially independent of the radial distance.

Radiative pumping of molecules is provided by thermal emission from hot dust close to the star. In molecular emission models this is usually represented by a blackbody of temperature  $T_{\text{BB}}$  and radius  $R_{\text{BB}}$ . These quantities can be estimated from the DRT-models. At each gridpoint in the DRT-model the blackbody temperature of the radiation field is determined. In this way a realistic estimate of  $T_{\text{BB}}$  and  $R_{\text{BB}}$  is obtained.

In G97 we showed that the near-infrared visibility curves are very sensitive to the grain size and that a main grain size of  $0.16 \pm 0.01 \mu\text{m}$  could fit the visibility curves. Therefore a grain size of  $0.16 \mu\text{m}$  is adopted in all calculations.

Finally, DRT-models provide  $\tau_{0.1}$ , the optical depth at  $1000 \text{ \AA}$  which is needed to calculate the photoelectric heating (see G94 for details) and the dust temperature profile which is needed in the heating rate due to the gas-dust temperature difference (see G94).

## 2.2. The outer radius and photodissociation

The outer radius of the CO shell is determined by photodissociation. Mamon et al. (1988) have investigated this effect and found that the CO abundance as function of radius, relative to the value close to the star, can be approximated as:

$$X_{\text{CO}} = e^{-\ln(2) (r/r_{1/2})^\alpha} \quad (5)$$

where  $r_{1/2}$  and  $\alpha$  depend on  $\dot{M}$  and  $v$  and are tabulated by Mamon et al. (1988). Here we instead use the analytical fit to these results by Stanek et al. (1995):

$$r_{1/2} = 5.4 \times 10^{16} \left( \frac{\dot{M}}{10^{-6}} \right)^{0.65} \left( \frac{v}{15} \right)^{-0.55} \left( \frac{f_{\text{CO}}}{8 \times 10^{-4}} \right)^{0.55}$$

$$+ 7.5 \times 10^{15} \left( \frac{v}{15} \right) \text{ cm} \quad (6)$$

and Kwan & Webster (1993)

$$\alpha = 2.79 \left( \frac{\dot{M}}{10^{-5}} \frac{15}{v} \right)^{0.09} \quad (7)$$

where  $f_{\text{CO}}$  is the number ratio of CO to  $\text{H}_2$  molecules close to the star,  $\dot{M}$  is the mass loss rate in  $M_\odot \text{ yr}^{-1}$  and  $v$  the gas velocity in  $\text{km s}^{-1}$ . The photodissociation radius of  $^{13}\text{CO}$  is to first approximation assumed to be equal to that of  $^{12}\text{CO}$  (see Mamon et al. 1988). The outer radius of the CO shell is set at the radius where the CO abundance has dropped to 1% in the calculations. Equations. (6) and (7) are used with a gas velocity of  $14.5 \text{ km s}^{-1}$ , which is the observed terminal velocity of the gas.

## 3. Best guesses for the dust-to-gas ratio and CO abundance

Two important free parameters are the dust-to-gas ratio and the abundance of CO molecules relative to  $\text{H}_2$ . Both quantities can not take arbitrary values.

There is a physical upper limit to the dust-to-gas ratio based on the number of atoms that can condense into dust. Using the continuity equation for the gas and the dust and assuming that the dust is 100% carbonaceous one finds that the theoretical dust-to-gas ratio is given by:

$$\Psi = f_c (C/O - 1) \frac{n_{\text{O}}}{n_{\text{H}}} \frac{12}{1.4} \frac{v_{\text{gas}} + v_{\text{dr}}}{v_{\text{gas}}} \quad (8)$$

where  $f_c$  is the degree of condensation of the dust and C/O is the number ratio of carbon to oxygen atoms in the gas phase. Taking the observed gas velocity of  $14.5 \text{ km s}^{-1}$ , and assuming a drift velocity of  $3.0 \text{ km s}^{-1}$  and a cosmic oxygen abundance of 8.70 (on a scale where H = 12.0) then the theoretically predicted dust-to-gas ratio is  $\Psi = 5.18 \times 10^{-3} f_c (C/O - 1)$ .

For disk planetary nebulae it found that  $C/O < 4$  (see e.g. Groenewegen & de Jong 1994 and references therein) and because  $f_c < 1$  by definition, it follows that  $\Psi$  must be smaller than 0.016. This upper limit is valid for all carbon stars. Calculations show that  $f_c$  is about 0.4 (within a factor of 2) (see Fleischer et al. 1995, Winters et al. 1994a,b) and for IRC +10 216 a C/O ratio of 2-3 seems appropriate (G97). In this case  $\Psi$  is in the range 0.001 - 0.008. In the model calculations we use dust-to-gas ratios between 0.001 and 0.005, in agreement with the theoretically expected range.

For  $f_{\text{CO}}$ , defined as the  $n(\text{CO})/n(\text{H}_2)$  ratio close to the star, one may assume that in a carbon star all oxygen atoms are locked up in CO. Using an oxygen abundance of  $8.70 \pm 0.1$  it immediately follows that  $f_{\text{CO}} = (10 \pm 2) \times 10^{-4}$ . All the best fitting models have derived CO abundances in this range. Note that some of the other models

**Table 4.** Fit to secondary constraints

Transition	Telescope	Observed Peak		Model Peak Temperature(K)				
		Temp. (K)	$L = 10\,000 L_{\odot}$	15 000	20 000	25 000	30 000	
$^{12}\text{CO}$ (1-0)	BTL	5.1	4.9	5.5	5.9	5.5	5.8	
	NRAO	9.6	9.3	10.3	10.9	10.3	10.8	
	SEST	10.7	10.2	11.2	11.9	11.2	11.7	
	OSO	10.0	13.2	14.7	14.9	14.2	14.5	
$^{12}\text{CO}$ (2-1)	NRAO	21.5	15.7	16.8	17.5	16.6	17.2	
	SEST	25.4	21.1	22.1	23.0	21.9	22.7	
$^{12}\text{CO}$ (3-2)	CSO	32.5	–	22.6	–	–	–	
$^{12}\text{CO}$ (7-6)	UH2.2	9.0	2.87	2.66	2.78	2.65	2.75	
$^{13}\text{CO}$ (1-0)	BTL	0.38	0.27	0.29	0.32	0.30	0.32	
$^{13}\text{CO}$ (3-2)	CSO	2.9 <sup>(a)</sup>	–	2.62	–	–	–	

<sup>(a)</sup> Wang et al. (1994) give a value of 3.9 K, but this apparently refers to the peak temperature of the horn, in this double-peaked profile. The observed temperature at the line center is read of their Fig. 2 and then appropriately scaled to give the main-beam temperature.

discussed in the literature (Kwan & Linke 1982, Crosas & Menten 1997) find a CO abundance of  $6 \times 10^{-4}$ , which is in disagreement with the theoretically expected value.

#### 4. The CO data

A wealth of CO data exist for IRC +10 216. In Table 1 we list the data that are used as constraints here. Except for the  $^{12}\text{CO}$  and  $^{13}\text{CO}$   $J = 6-5$  spectra, all data are taken from the literature.

The  $^{12}\text{CO}$  and  $^{13}\text{CO}$   $J = 6-5$  observations were carried out using the James Clerk Maxwell Telescope (JCMT), located on Mauna Kea, Hawaii. The detector was an SIS receiver (RxG) available to JCMT via a collaborative agreement with the Max-Planck-Institut für Extraterrestrische Physik in Garching (Germany). A Gunn oscillator yields continuous coverage across the 650-692 GHz band, which includes the  $^{12}\text{CO}$  and  $^{13}\text{CO}$   $J = 6-5$  lines. The backend was an acousto-optic spectrometer. Before the observations were made, the planets Jupiter and Mars were used to determine the beamshape during good weather with a 30% zenith transmission. It was found that, although the JCMT beam is complex at these high frequencies, it can be well described by a two-component beam with 55% of the power in the 7'' FWHM diffraction component and 45% of the power in a 18'' FWHM beam. The overall beam efficiency in this compact beam is 27% and was determined by taking spectra of Jupiter and Mars. When taking all errors into account we expect the calibration error to be less than 20%.

The  $^{12}\text{CO}$   $J = 6-5$  observations were made on April 21 and 25, 1995. The pointing was done using the continuum receiver UKT14. The relative pointing difference between the RxG and UKT14 receivers was determined using very bright sources and was accurately known. After the telescope was successfully pointed at the source using UKT14, a switch was made to RxG and the relative pointing cor-

rection was applied. During the observations IRC +10 216 was always above 70 degrees elevation. The zenith sky transmission was 17% on April 21 and 19% on April 25 yielding system temperatures of 17 000 and 22 000 K respectively. Four scans of 4 min each were made, three of which were on April 21, for a total integration time of 16 min. On April 21 the on-source spectra were part of a 5-point map with a beam separation of 8''; on April 25 the on-source spectrum was part of a 5-point map with a 10'' beam separation.

In Figs. 1-5 one can notice a bump in the spectrum centered near a velocity of 0 km s<sup>-1</sup>. It is not present in the  $J = 6-5$  spectrum of Crosas & Menten (1997). We checked the JPL line catalog and no suitable candidate could be found. We also checked for lines coming in from the sideband with the same result. In any case this unidentified line does not influence any conclusions regarding the (fitting of the)  $J = 6-5$  profile.

The  $^{13}\text{CO}$   $J = 6-5$  observations were made on April 30, 1995. The pointing was done as described above for the  $^{12}\text{CO}$  observations. During the observations IRC +10 216 was between 65 and 70 degrees elevation. The zenith sky transmission was 32% yielding a system temperature of 10 000 K. Seven scans of 8 min each were made for a total integration time of 56 min. No mapping was done in this line.

The above data were added after visual inspection of the individual scans and base line subtraction. The rms noise in the final  $^{12}\text{CO}$   $J = 6-5$  spectrum is 2.4 K while the line is about 45 K. The rms noise in the final  $^{13}\text{CO}$   $J = 6-5$  spectrum is 0.8 K while the line is about 7 K.

The primary constraints in this paper are the  $J = 6-5$  profiles discussed above, the  $^{12}\text{CO}$   $J = 4-3$  profiles from Williams & White (1992) and  $^{12}\text{CO}$  and  $^{13}\text{CO}$   $J = 1-0$ , 2-1 and 3-2 profiles observed at IRAM and JCMT and discussed in Groenewegen et al. (1996). In addition a se-

lection of other data was taken from the literature in particular that taken with smaller telescopes.

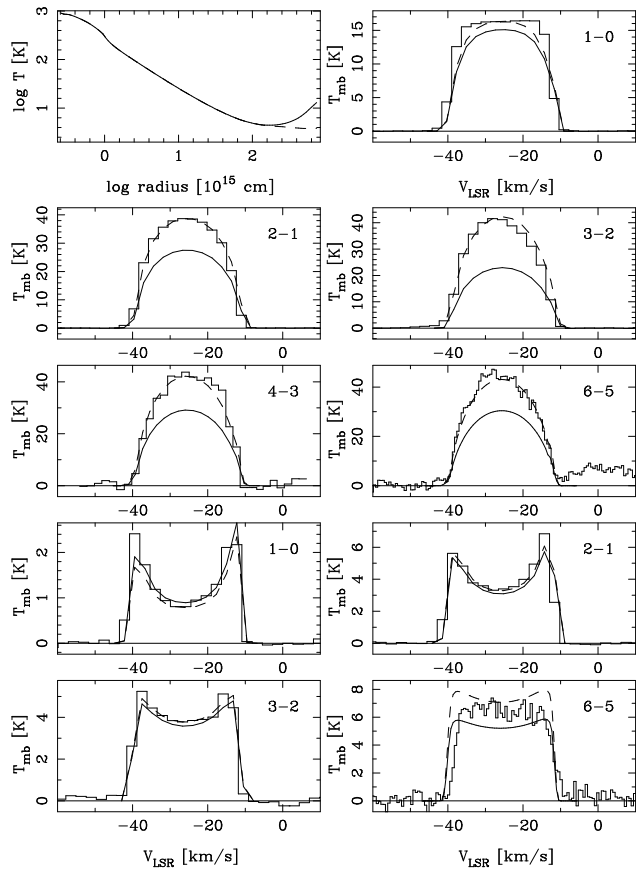


**Fig. 1.** Model with  $L = 10\,000 L_{\odot}$ , and default parameters for  $\dot{M}$ ,  $\Psi$  and  $Q$ . Upper left panel indicates gas temperature (solid line) and excitation temperature of the  $^{12}\text{CO}$  (1-0) transition (dashed line). The rise in the gas temperature at large distances from the star is due to photoelectric heating. Other panels indicate  $^{12}\text{CO}$  (upper part) and  $^{13}\text{CO}$  (lower four panels) line profiles. In each case the histogram indicates the observations. They are the “primary constraints” of Table 1. The solid line indicates the model, while the dashed line represents the model scaled to the observed maximum, in order to better compare the line shapes.

## 5. Model calculations

A large grid of models was calculated, varying the luminosity (and the distance correspondingly), the mass loss rate, the dust-to-gas ratio, the absolute dust opacity and  $f_{\text{CO}}$  while fixing  $f_{\text{CO}}/f_{13\text{CO}}$  at a value of 44, a value accurately known from optically thin molecular lines (see Kahane et al. 1992). The velocity law of the gas is parameterised by  $v(r) = 14.5 \text{ km s}^{-1} (1 - 2.73 \times 10^{14} \text{ cm } (d/135 \text{ pc})/r)^{0.5}$ .

From the dust modeling in G97 the following parameters were derived:  $Q = 0.0419$ ;  $a = 0.16 \mu\text{m}$ , inner (dust)

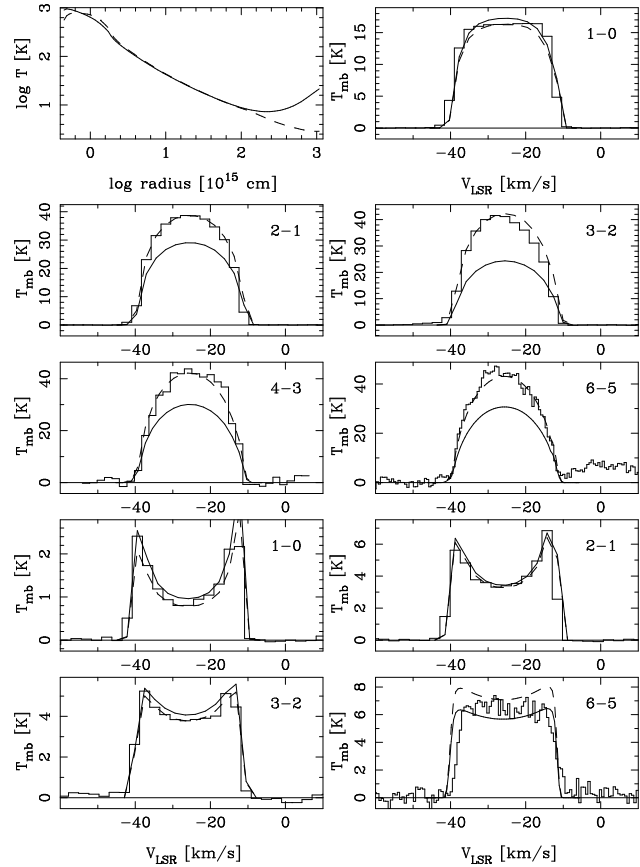


**Fig. 2.** Model with  $L = 30\,000 L_{\odot}$ , and default parameters for  $\dot{M}$ ,  $\Psi$  and  $Q$ .

radius  $= 3.17 \times 10^{14} \text{ cm}$  ( $d/135 \text{ pc}$ );  $T_{\text{BB}} = 860 \text{ K}$ ;  $R_{\text{BB}} = 6.18 \times 10^{14} \text{ cm}$  ( $d/135 \text{ pc}$ );  $\tau_{0.1} = 1.84 \times 10^{16} \text{ cm}$  ( $d/135 \text{ pc}$ )/ $r$ , with  $r$  the radial distance to the star. Given the observed integrated flux, Table 2 lists the distance corresponding to several chosen values of the luminosity, and the mass loss rate following from the dust model.

The actual combinations of parameters used in the various CO model calculations are listed in Table 3. For example, take the entry with  $L = 20\,000 L_{\odot}$ , “ $\dot{M}_{\text{def}}/1.4$ ” and “ $\Psi/1.67$ ”. The default mass loss rate for that luminosity is  $2.54 \times 10^{-5} M_{\odot} \text{ yr}^{-1}$ , and the default dust-to-gas ratio is 0.005 (see Table 2). This therefore means that the model was run with  $\dot{M} = 1.81 \times 10^{-5} M_{\odot} \text{ yr}^{-1}$  and  $\Psi = 0.0030$ . From Eq. (3) it follows that the dust opacity was  $(1.4 \times 1.67) \times 68 = 160 \text{ cm}^2 \text{ gr}^{-1}$ . For every model combination the CO abundance ratio was tuned to give the best possible fit to both the  $^{12}\text{CO}$  and  $^{13}\text{CO}$  line profiles marked as “primary constraint” in Table 1. The  $^{13}\text{CO}$  abundance was fixed at  $(f_{\text{CO}}/44)$  as explained above.

Figures 1-2 present the fits to the “primary constraints” for models with the default values for the mass loss rate, opacity and dust-to-gas ratio for the two extreme luminosities. Larger luminosities result in higher predicted brightness temperatures. This is most clearly seen in the

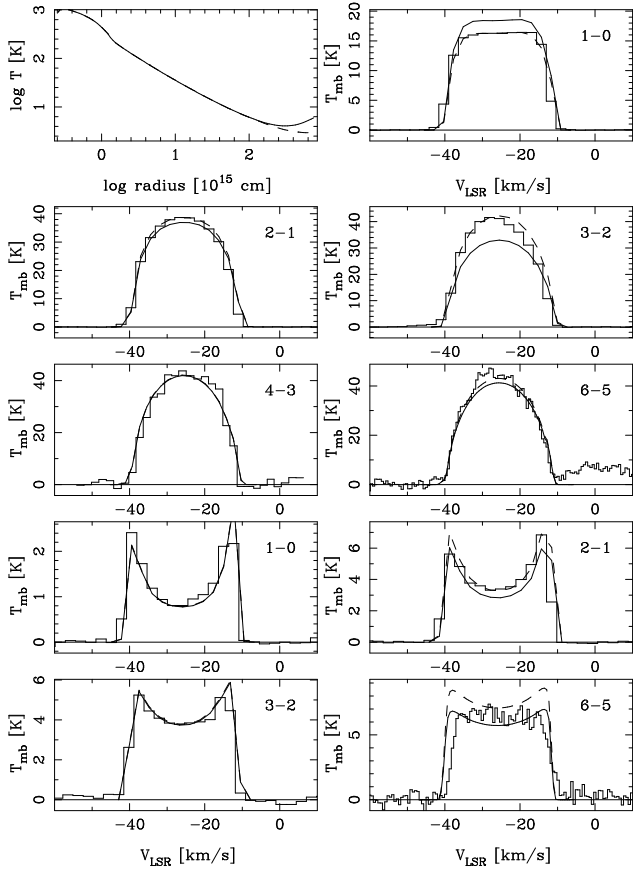


Fig. 3. Best fitting model with  $L = 10\,000 L_{\odot}$ .

$^{12}\text{CO}(1-0)$  profile. Overall however, the effect of luminosity appears not be very significant, and therefore only the extreme models with  $L = 10\,000$  and  $30\,000$  are shown. It is also clear that these models (and the models with intermediate luminosities) fail to fit the “primary constraints”.

Figures 3-5 present the best fitting models for three different luminosities. These models have a bold-faced entry in Table 3. For every luminosity a model can be found that fits the “primary constraints” almost equally well. The high-luminosity models are not shown because they fit qualitatively equally good, and such high luminosities can be ruled out on other grounds (see later). In all cases the models predict brightness temperature for the  $^{12}\text{CO}$  (3-2) line that is too low. This may indicate a systematic uncertainty in the calibration (also see discussion in Sect. 5.1.1). Also, all the models predict a  $^{12}\text{CO}$   $J = 1-0$  line that is too bright. This difference is lowest for the  $10\,000 L_{\odot}$  model, where the difference is well within the calibration uncertainty. The remaining discrepancy is the  $^{13}\text{CO}$  (6-5) line. The absolute intensity is well reproduced but the line shape does not fit very well. None of the models calculated predict a flat-topped  $^{13}\text{CO}$  (6-5) line. Also the recent model calculation of Crosas & Menten (1997)

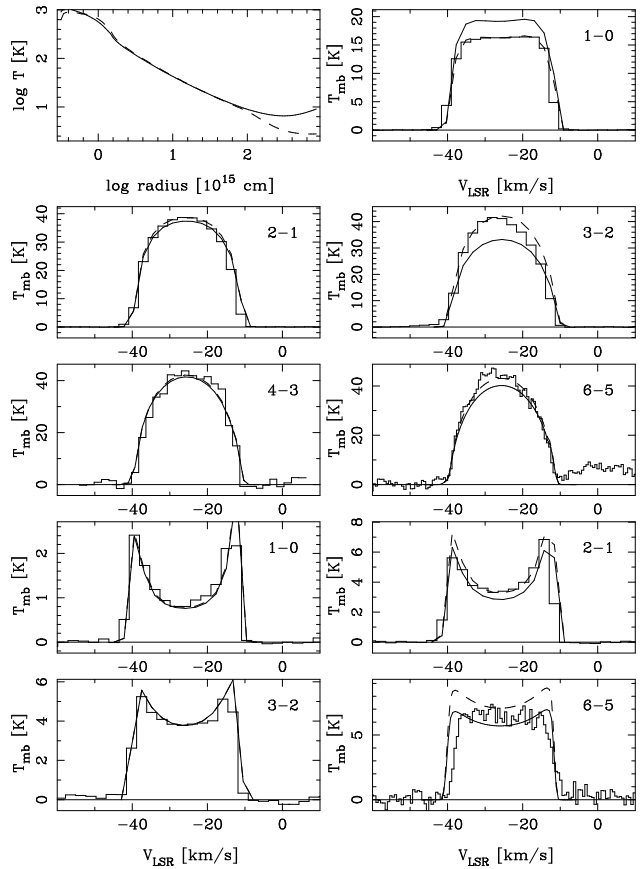


Fig. 4. Best fitting model with  $L = 15\,000 L_{\odot}$ .

predicts a slightly double-peaked profile. Note that their model does not reproduce the absolute intensity neither.

It was verified that this discrepancy is not due to a pointing off-set. A model calculated  $3.5''$  off-centre still produced a slight double-peaked profile. A model at  $7''$  off-set produced a flat-topped profile but the absolute intensity was a factor of 3 below the observed one.

This discrepancy hints to the fact that possibly one of the fundamental assumptions in the model may no longer be full-filled: spherical symmetry or homogeneity. This can in principle be addressed by high spatial resolution, high frequency mapping observations. Problems associated with these high frequency observations are that the beam is usually small, and random pointing errors can already be a significant fraction of the primary beam, and the influence of the error beam, which makes interpretation not straightforward.

### 5.1. The other constraints

#### 5.1.1. On-source data

We compared the best fitting model at each luminosity with the line intensities and line profiles for all on-source observations that were not used as primary constraints



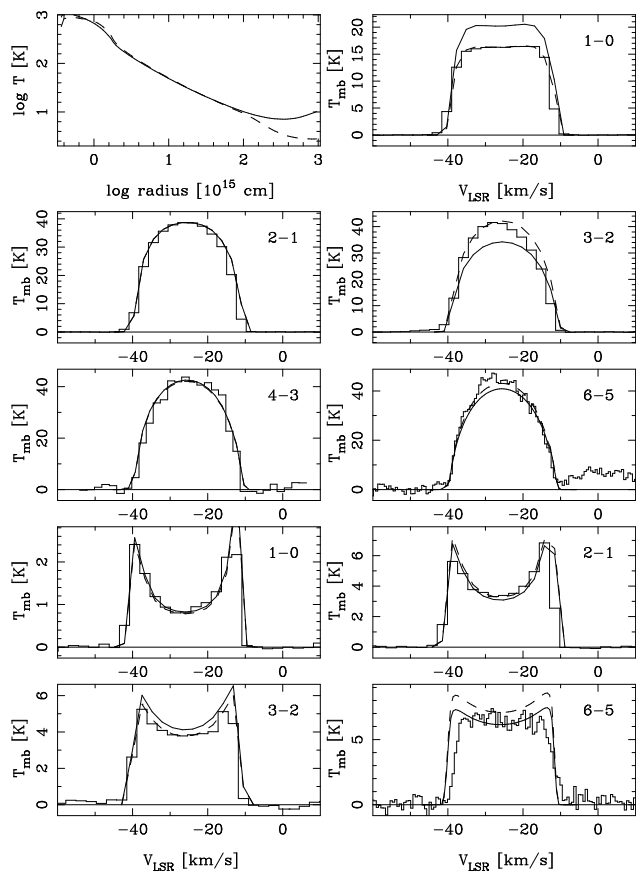


Fig. 5. Best fitting model with  $L = 20\,000 L_{\odot}$ .

(see Table 1). The peak intensities predicted by the model are listed in Table 4, together with the observational data from the respective papers.

The reasoning behind this exercise is that these other  $J = 1-0$  and  $2-1$  observations were performed with smaller telescopes with large beam sizes, and so these observations sample a greater extent of the envelope than the higher resolution IRAM observations.

The  $J = 1-0$  BTL, NRAO and SEST data are equally well fitted by the five models, given the typical  $1\sigma$  uncertainties of 10% in the observations. In fact, all three observations would point to a luminosity between 10 000 and 15 000  $L_{\odot}$ . Regarding the OSO observations there must have been a calibration error. Indeed, Huggins et al. mention that no beam efficiency correction is applied and that the observations have been scaled to an earlier 1982 OSO observation. A more recent OSO observation (Olofsson et al. 1993) indicates a peak temperature of 12.5 K which is low but formally in agreement with the models. The  $^{13}\text{CO}$   $J = 1-0$  BTL observation agrees reasonably well with the models.

The  $J = 2-1$  NRAO observations are barely in agreement with the models. Other NRAO observations find similarly high on-source temperatures (Wannier & Sahai

1986, Wannier et al. 1990). The SEST data agrees with the models.

With respect to the  $J = 7-6$  observations there is a discrepancy of more than a factor of three. We have no explanation for this. This is the only existing  $7-6$  observation of this star, and we suggest that this transition be re-observed. As the  $J = 6-5$  data is well fitted, there is no reason to believe that our model is in error by such a large factor.

The referee kindly pointed us to the paper of Wang et al. (1994) which was not considered originally and discusses  $^{12}\text{CO}$  and  $^{13}\text{CO}$  ( $3-2$ ) data taken with the CSO. For one model, the relevant temperatures were calculated, and are included in Table 4. The  $^{13}\text{CO}$  ( $3-2$ ) model prediction is in excellent agreement with the observation, while the  $^{12}\text{CO}$  ( $3-2$ ) model prediction is significantly lower.

Williams & White (1992) also present  $^{12}\text{CO}$  and  $^{13}\text{CO}$  ( $3-2$ ) data taken with the JCMT, and can therefore be directly compared to our observations. For the  $^{12}\text{CO}$  line they find a main-beam temperature of 32 K at  $2''$  offset, and estimated an on-source temperature of about 37 K. We find 41 K, in excellent agreement. For  $^{13}\text{CO}$  they find a line-center temperature of 3 K (at a position  $\pm 5''$ ), while we found 3.8 K. This agreement is acceptable, and it should be pointed out that their spectrum has a considerable lower S/N than ours.

In conclusion, the two sets of JCMT data are in agreement with each other. For both CSO and JCMT the predicted  $^{12}\text{CO}$  ( $3-2$ ) line is less intense than observed. The same is found by Crosas & Menten (1997) who compare their model to the Wang et al. data and find a model temperature in agreement with our value in Table 4 and hence lower than observed. In Sect. 5.0 it was suggested that this might be due to a calibration problem. This would imply calibration problems at both CSO and JCMT, which appears unlikely. On the other hand a physical cause also appears unlikely. As temperature and density are smooth functions of radius, the profiles are also expected to be smooth function of increasing J-level. Since the  $^{12}\text{CO}$   $J=2-1$  and  $4-3$  levels are well fitted, there is no a-priori reason to believe that the  $3-2$  level would be off. One could assume that at a radius, where the emission from the  $3-2$  level is strongest, the density is lower than predicted from the standard model, but this would also then imply a different  $^{12}\text{CO}/^{13}\text{CO}$  ratio at that particular radius only as the  $^{13}\text{CO}$   $3-2$  profile is predicted correctly.

### 5.1.2. Mapping data

In Fig. 6 the four best fitting models are compared to the mapping data of Huggins et al. (1988), Truong-Bach et al. (1991) and Groenewegen & Ludwig (1998), both on a linear and logarithmic scale. For the IRAM observations integrated intensities are compared, while for the OSO and NRAO observations by Huggins et al. only peak intensities are given in their paper. There exists a map in the  $^{12}\text{CO}$

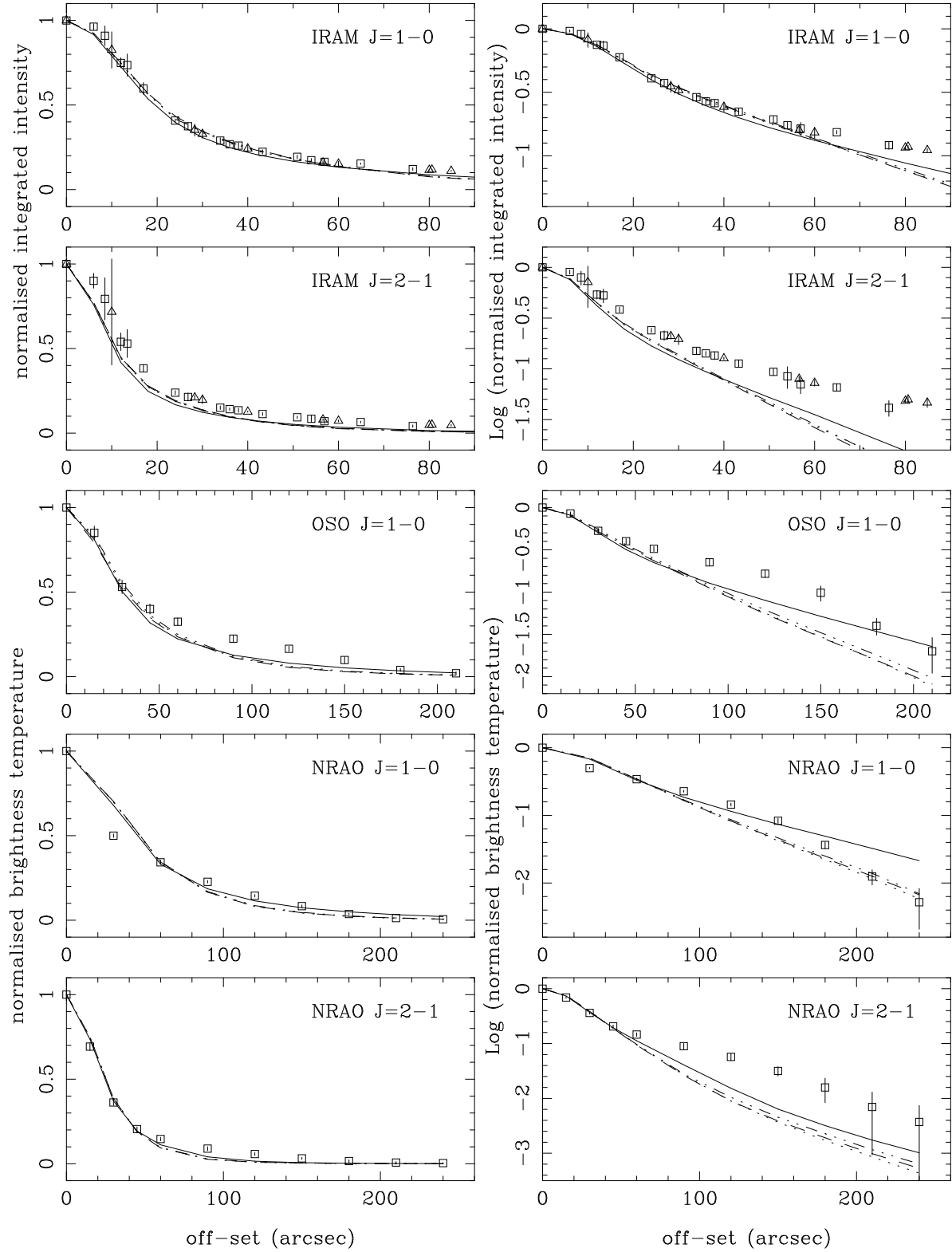


**Fig. 6.** Comparison between observations (symbols with error bars) and models (lines) as a function of radial offset. IRAM observations come from Truong-Bach et al. (1991; squares), and Groenewegen & Ludwig (1998; triangles). The OSO and NRAO observations are from Huggins et al. (1988). Best fitting models are for  $L = 10\,000$  (solid),  $15\,000$  (dashed),  $25\,000$  (dotted),  $30\,000 L_{\odot}$  (dash-dot-dot-dotted), and default values for photoelectric heating and constant mass loss rate. For the IRAM observations normalised integrated intensities, and for the OSO/NRAO observations normalised peak brightness temperatures are shown, on both a linear (left hand) and logarithmic scale (right hand).

J = 3-2 line (Williams & White 1992), but they find that the emission appears not to be extended with respect to the beam out to their maximum off-set of  $50''$ . Therefore we did not consider this data.

A first remark is that there is extremely good agreement between the two sets of IRAM observations. The error bars plotted indicate the variation in the ratio of the integrated intensity relative to the on-source value at the different map positions for a given radial offset.

At first glance there appears to be good agreement between the models and observations when plotted on a linear scale, but, as was noted by Huggins et al. (1988), clear discrepancies are seen when plotted on a logarithmic scale. Although the absolute calibration uncertainties are of order 10% (and larger in the case of the OSO J = 1-0 observation), the relative intensities are much better determined and only limited by noise.

The models and observations start to deviate at approximately  $50''$  offset from the center position, the exact value depending on the beam-size. There are two possible explanations for this. First, the mass loss rate may have been higher in the past. Second, the photoelectric effect may be more important than assumed.

Models with an increased mass loss in the past have been constructed to fit the data for luminosities of 15 000 and 30 000  $L_{\odot}$ . A good fit is obtained when the mass loss rate is higher by a factor of 5 for radial offsets  $\gtrsim 50''$ . These models are shown in Fig. 7 on a logarithmic scale only. The fit to the IRAM data is very good. That to the NRAO J = 2-1 and OSO J = 1-0 data is acceptable. On the other hand there is an obvious discrepancy between the OSO and NRAO J = 1-0 data. In the present model we assumed that the increase in the mass loss rate is constant and extends to the outer radius. Given the presently available relatively poor data for radial offsets  $\gtrsim 90''$ , and the discrepancies for radial offsets  $\gtrsim 150''$ , it can not be excluded that the mass loss rate is lower again in the outer parts of the envelope. The error in the radius of the on-set of the enhanced mass loss rate and the factor by which this is so are approximately  $10''$  and less than a factor of 2, respectively. From the radial dependence observed with IRAM compared to the constant mass loss rate case it is immediately clear that there is a break in the observations between 40 and  $60''$ . It was verified numerically that a model with an increase in mass loss rate of a factor of 3 did not fit the data. Although we do not claim that our best-fitting model is unique, this gives some constraints on the associated uncertainties of this model.

As the increase in the mass loss rate occurs at offsets much larger than the respective beam sizes, negligible changes are expected in the on-source fluxes. This was verified numerically.

Models with increased photoelectric heating were also considered (for the case of a constant mass loss rate and  $L = 15\,000 L_{\odot}$ ). Even a model with the parameter ( $G \times Y$ ; see Sect. 2) a factor six larger than the default value could

not fit the IRAM data, although it could fit some of the NRAO/OSO data. The reason is, that for the photoelectric effect to be important even at  $50''$  from the star the interstellar radiation field must be very strong. Apart from the fact that the model with increased photoelectric effect does not fit the IRAM data, such a model appears also unphysical, as for a distance of 150 pc and its galactic latitude IRC +10 216 is at 110 pc from the galactic plane, where one does not expect an increase in the diffuse interstellar radiation field by such a large amount.

## 6. Visibility curves

In principle, interferometric observations yield additional information on the structure of the circumstellar envelope. In an article in the JCMT newsletter, Hills (1996) briefly mentions that interferometric observations at the wavelength of the J = 4-3 line had been performed with the JCMT-CSO interferometer. To provide comparison with future observations, we have calculated the so-called visibility curves at the center wavelengths of the J = 1-0 up to 6-5  $^{12}\text{CO}$  transitions for the best fitting models with constant mass loss rate. For a brief summary on what a visibility curve is, and how they are evaluated, we refer to Sect. 2.1 of G97. The results of the calculations are plotted in Fig. 8.

The model with mass loss variations as described above yield results indistinguishable from the constant mass loss rate case. This is due to the fact that these mass loss variations occur at large radii.

At the same time this implies that the visibility curves may be most sensitive to the geometry of the CO shell. Asymmetries would be revealed by obtaining the visibility curves for different position angles.

## 7. Discussion

### 7.1. General comments

We have made the most consistent modelling of the CO and dust envelope around IRC +10 216 so far. In particular we did not assume that the gas-dust momentum transfer rate is a free parameter but constrained it from our previous dust modelling. The physical range of the dust-to-gas ratio and the CO abundance are considered, contrary to some other models that find unrealistically low values for the CO abundance.

Contrary to Sahai (1987) and Truong-Bach et al. (1991), and in agreement with Crosas & Menten (1997), we find no evidence for a hot core in the inner  $6''$  region. Specifically with respect to the Truong-Bach et al. result, Crosas & Menten suggest that they took too few rotational levels into account and therefore underestimated the rotational cooling in the inner part. Truong-Bach et al. inference was based on an old J = 6-5 observation (Koepl et al. 1982). For the best-fitting  $15\,000 L_{\odot}$  model we find a

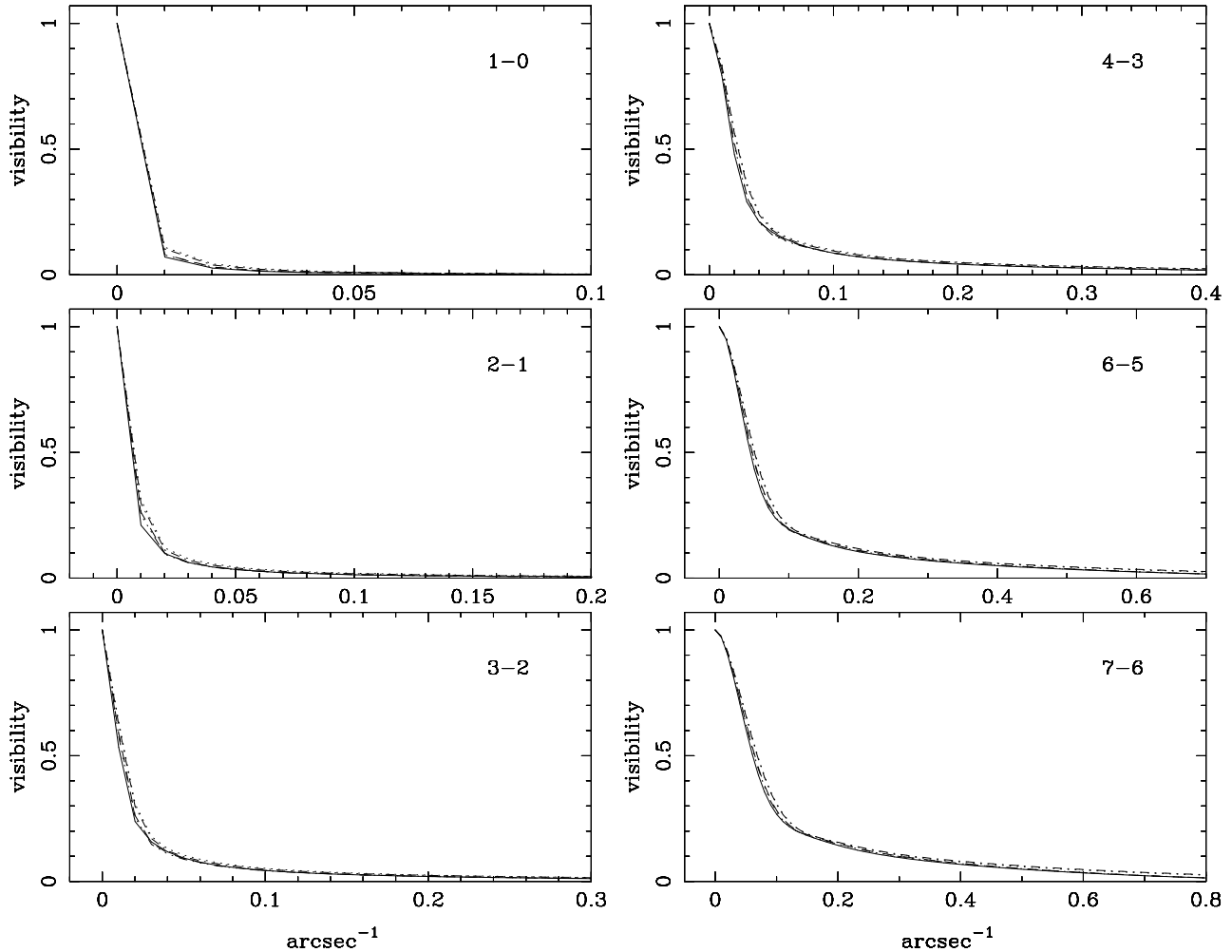


**Fig. 8.** Visibility curves for the best fitting models with constant mass loss rate,  $L = 10\,000$  (solid),  $15\,000$  (dashed),  $20\,000$  (dot-dashed),  $25\,000$  (dotted),  $30\,000$   $L_{\odot}$  (dash-dot-dot-dotted), for different transitions. The calculations are performed with a resolution of  $0.01$   $\text{arcsec}^{-1}$ .

peak temperature of  $5.6$  K in the corresponding  $35''$  beam, almost a factor of three below the reported value.

Cernicharo et al. (1996) discuss an ISO LWS grating observation of IRC +10 216. On top of the dust continuum there is a forest of HCN and CO lines. They infer that temperatures of order  $700$ - $1500$  K are needed to explain these observations. Specifically they adopt a temperature of  $1200$  K for radii smaller than  $6 \times 10^{14}$  cm. From our self-consistent temperature determination we find a gas temperature at the inner radius ( $3.2 \times 10^{14}$  cm for a distance of  $135$  pc) of  $1100$  K. This agreement is encouraging.

In Groenewegen et al. (1997) we mapped IRC +10 216 in the  $1.3$  mm continuum and found evidence for phases of enhanced mass loss in the past at radial distances of  $5$  and  $20''$  from the star. Although we find evidence for a higher mass loss rate in the past from the CO observations, the radial scales are different. This is not necessarily incompatible. First, the largest variation found from the

continuum map is only a factor of two at most and takes place from  $10$  to  $30''$  at most. This may be not detectable in the CO. Secondly, as the continuum emission is detected at a significant level only out to  $45''$  it is not possible to prove or disprove if the variations seen in CO are also seen in the continuum emission.

### 7.2. The influence of the radial dependence of $Q$

Crosas & Menten (1997) find that they require a higher value for  $Q$  in the inner region, specifically  $Q = 0.025$  for  $r \lesssim 10^{16}$  cm (that is 20 times their inner radius) and  $Q = 0.018$  for  $r > 10^{16}$  cm. This touches upon the expectation (see Sect. 2.1) that  $Q$  should be a function of distance to the star because the effective wavelength of the emerging spectrum is shifting to longer wavelength due to the influence of dust. Crosas & Menten claim that their adopted behaviour for  $Q$  is in agreement with recent calculations, e.g. Habing et al. (1994), which showed that

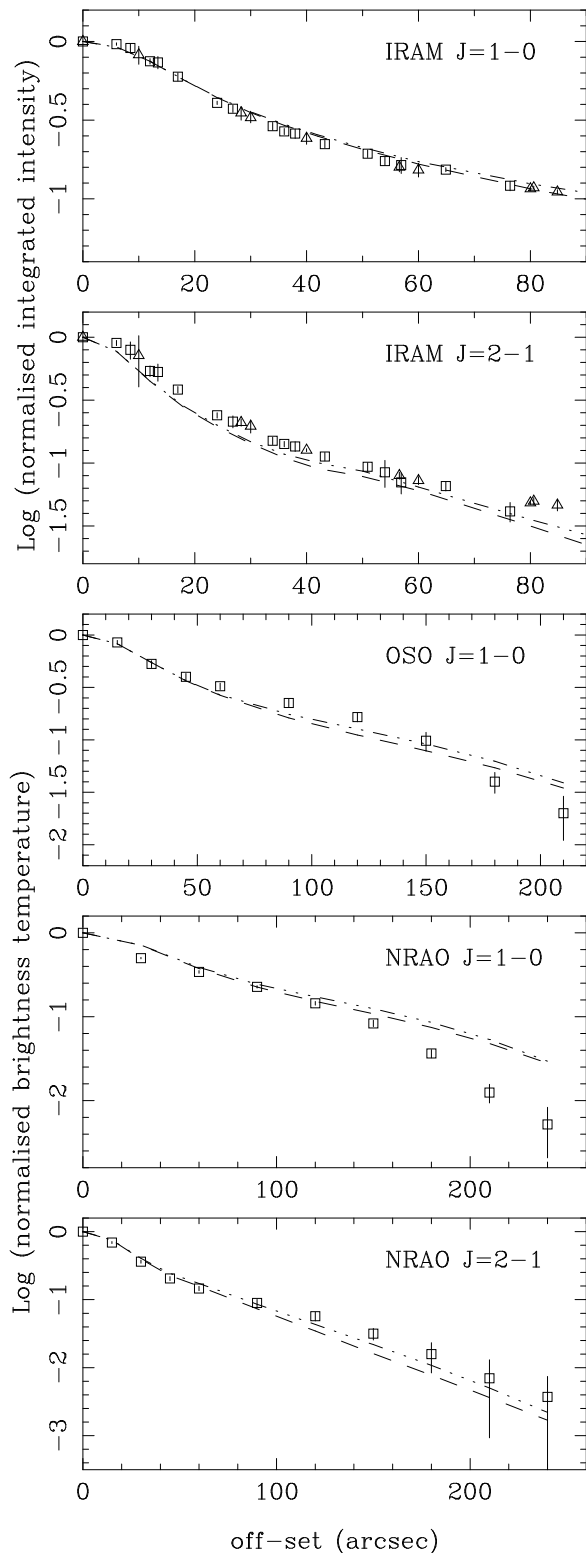


**Fig. 7.** As previous figure but now for models including a higher mass loss rate in the past, as discussed in the text.  $L = 15\,000$  (dashed),  $30\,000 L_{\odot}$  (dash-dot-dot-dotted).

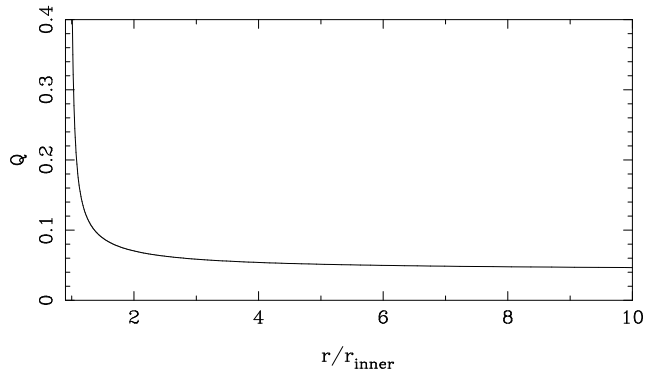


**Fig. 9.** Radial dependence of the gas-dust momentum transfer efficiency  $Q$ .

$Q(r)$  is a strongly decreasing function of  $r$ . We in fact took the results by Habing et al. to assume a constant  $Q$  throughout the envelope. We will now address the influence of this assumption by taking the radial dependence of  $Q$  into account. Figure 9 shows the radial dependence of  $Q$  as calculated from the best-fitting dust model. It shows that  $Q$  is rapidly dropping from large values to a value of 0.0419 adopted in all calculation so far. However, and contrary to the argument used by Crosas & Menten, it is clear that  $Q$  starts to deviate from its value at infinity only for radial distances much smaller than  $10^{16}$  cm. In Table 5 on-source peak temperatures for various  $^{12}\text{CO}$  transitions are collected for the best-fitting model with  $L = 15\,000 L_{\odot}$ , and different assumptions about  $Q$ . The list includes the  $J = 9-8$  and  $12-11$  transitions which can not be measured from the ground, but can be from space. Shown are the standard case with a constant  $Q$  down to the inner radius, and various models where the radial dependence of  $Q$  is taken into account down to a certain inner radius. For inner radii smaller than  $5 \times 10^{14}$  cm the model experiences some convergence problems. Since a greater value for  $Q$  means more heating (see Eq. 1) it is expected that models which take into account the radial dependence of  $Q$  lead to higher temperatures in the inner region and hence more emission from the high- $J$  transitions.

The result of the calculations show two things. For the low- $J$  transitions, where the radial dependence of  $Q$  should be of no importance since the excitation temperatures are low, it is important to choose the inner radius not too big as this will result in an underestimate of the brightness temperature. This might also be part of the explanation for the need of an inner hot core by Truong-Bach et al. They assumed an inner radius of  $2''$  or  $6.0 \times 10^{15}$  cm for their adopted distance. This results in an underestimate of the true brightness temperature. If they had chosen a smaller inner radius (equal to the inner dust radius, which is in fact a physically plausible choice) the need, if any, for a hotter inner core would have been less.

For the  $J = 3-2$  and  $4-3$  transition the effects are smaller than 5% in the present case. The  $J = 7-6$  result

**Table 5.** Influence of the radial dependence of  $Q$ . On-source peak temperatures for various transitions.

Transition	Beam (")	$r_{\text{inn}} = 3.2 \times 10^{14}$ cm $Q(r_{\text{inn}}) = 0.0419$	$3.2 \times 10^{15}$ 0.0466	$1.7 \times 10^{15}$ 0.0503	$7.9 \times 10^{14}$ 0.0629	$5.0 \times 10^{14}$ 0.0838
1-0	21	$T_{\text{mb}} = 19.2$	18.3	18.9	19.1	19.2
2-1	12.5	37.4	32.9	36.2	37.9	38.2
3-2	14.3	33.2	29.4	32.1	34.0	34.4
4-3	11.0	41.4	34.5	38.8	42.5	43.6
6-5	7.0	62.0	45.0	54.2	63.8	67.3
7-6	45	2.7	2.4	2.6	2.8	2.9
9-8	80	0.53	0.43	0.49	0.56	0.59
12-11	60	0.55	0.37	0.46	0.58	0.63

shows that the effect becomes important for higher levels, and smaller beam sizes. As the high-J levels are generally measured with large beams, the effects are again moderate (of order 10%).

### 7.3. The overall best fit

Can a best model be identified? Not from the dust modelling alone as is mentioned in G97, since the shape of the spectral energy distribution is determined by the optical depth and the luminosity is a scaling parameter (see Table 2). The reason to consider CO observations as well, is that the heating rate is a non-linear function of luminosity (see Eq. 1). It turns out that for a plausible range of luminosities an almost equally best-fitting model to the primary constraints can be found.

Some of the published CO J = 1-0 observations point to a luminosity  $\lesssim 15\,000 L_{\odot}$ . An independent constraint is the period-luminosity relation for carbon miras (Groenewegen & Whitelock 1996). For a period of 649 days (Le Bertre 1992) it implies a luminosity of  $9850 L_{\odot}$ . The uncertainty in the period of about 10 days implies an uncertainty of about  $150 L_{\odot}$ . The uncertainty in the fit itself is 0.26 in  $m_{\text{bol}}$  which implies an error of 30% in luminosity. Thus from the  $PL$ -relation one derives therefore a luminosity between 7 700 and 12 500  $L_{\odot}$ .

An additional constraint comes from the observed terminal gas velocity. The assumption that radiation pressure on dust drives the outflow puts constraints on the mass loss rate and other parameters. Basically the formula  $\dot{M} (v_{\infty} - v_0) = \tau_{\text{F}} \frac{L}{c} (1 - \frac{1}{\Gamma})$  must be obeyed (see Netzer & Elitzur 1993, Ivezić & Elitzur 1995, Groenewegen et al. 1998), with  $v_0$  the gas velocity at the inner radius,  $\tau_{\text{F}}$  the flux-weighted optical depth (known from the DRT modelling), and  $\Gamma$  is the ratio of radiation pressure to gravitational pull which scales like  $\Gamma \sim \frac{Q L \Psi}{a \rho_{\text{d}} M_{\star}} \frac{v_{\infty}}{v_{\infty} + v_{\text{drift}}}$ . Details on how this system of equations is solved iteratively is explained in Groenewegen et al. (1998). The equation allows one to verify that the mass loss rate and dust-to-gas ratio derived from the CO modelling are consistent with those derived from the DRT modelling using the above equation

and procedure. Unknowns are the mass of the star ( $M_{\star} = 0.8 M_{\odot}$  adopted), the gas velocity at the inner radius ( $v_0 = 1 \text{ km s}^{-1}$  adopted). The dust opacity is the one given by the best-fitting CO model for each luminosity. The results are listed in Table 6.

**Table 6.** Comparison between CO and infrared modelling

Lum. ( $L_{\odot}$ )	$\kappa_{60\mu\text{m}}$ $\text{cm}^2/\text{gr}$	$M_{\text{CO}}$ $M_{\odot}/\text{yr}$	$\Psi_{\text{CO}}$ $10^{-2}$	$M_{\text{IR}}$ $M_{\odot}/\text{yr}$	$\Psi_{\text{IR}}$ $10^{-2}$
10 000	326	$1.50 \times 10^{-5}$	0.125	$1.10 \times 10^{-5}$	0.137
15 000	245	$1.83 \times 10^{-5}$	0.167	$1.73 \times 10^{-5}$	0.135
20 000	245	$2.11 \times 10^{-5}$	0.167	$2.37 \times 10^{-5}$	0.113
25 000	283	$3.40 \times 10^{-5}$	0.100	$3.02 \times 10^{-5}$	0.099
30 000	204	$3.11 \times 10^{-5}$	0.167	$3.67 \times 10^{-5}$	0.104

The uncertainty in the mass loss rate and dust-to-gas ratio derived from the dust shell is about 8% and 6% due to uncertainties in the assumed mass (varied to  $0.6 M_{\odot}$ ) and  $v_0$  (varied to  $0 \text{ km s}^{-1}$ ). In the ideal situation the mass loss rates and dust-to-gas ratios from the two methods would be identical to indicate a perfectly consistent model. The best overall agreement based on this analysis is achieved for a luminosity of  $15\,000 L_{\odot}$ .

Given all these considerations it is likely that the luminosity of IRC +10 216 is between  $10\,000$  and  $15\,000 L_{\odot}$  and its distance is between 110 and 135 pc. The present-day mass loss rate is  $(1.5 \pm 0.3) \times 10^{-5} M_{\odot} \text{ yr}^{-1}$  and the gas-to-dust ratio is about  $700 \pm 100$ . The dust opacity at  $60 \mu\text{m}$  is found to be of order  $250 \text{ cm}^2 \text{ gr}^{-1}$ . The CO abundance is  $1.1 \times 10^{-3}$  relative to  $\text{H}_2$ .

Compared to the previously proposed models mentioned in the introduction this represents a somewhat lower mass loss rate, partly because these other models adopted larger distances as well in many cases. The CO abundance is larger than in most previous models, but in agreement with theoretical expectations.

The gas-to-dust ratio we find is larger than the canonical value of 200 often quoted. On the other hand there have been other recent studies that found larger gas-to-dust ratios for carbon stars as well, e.g. a gas-to-dust ratio of 550 for IRC +10 216 for a distance of 135 pc (Ivezić & Elitzur 1996), a value of 1230 for IRC +10 216 (Winters et al. 1997b), a value of 530 for AFGL 3068 (Winters et al. 1997a). Note that in the model of Crosas & Menten (1997) the gas-to-dust ratio is fixed at 100, and they mention that a larger value would result in lines that are consistently too low.

*Acknowledgements.* Dr. Truong-Bach kindly made available the IRAM J = 1-0 and 2-1 data described in Truong-Bach et al. (1991). We would like to thank John Howe, Mark Heyer, Linda Tacconi, Andy Harris and Reinhard Genzel, who were involved to some extent in the CO (6-5) observations. This research has made use of the SIMBAD database, operated at CDS, Strasbourg, France. vspace=0.3mm

## References

- Cernicharo J., Barlow M.J., González-Alfonso E., et al., 1996, A&A 315, L201  
 Crosas M., Menten K.M., 1997, ApJ 483, 913  
 Fleischer A.J., Gauger A., Sedlmayer E., 1995, A&A 297, 543  
 Groenewegen M.A.T., 1994a, A&A 290, 531 (G94)  
 Groenewegen M.A.T., 1994b, A&A 290, 544  
 Groenewegen M.A.T., 1996, A&A 305, L61  
 Groenewegen M.A.T., 1997, A&A 317, 503 (G97)  
 Groenewegen M.A.T., de Jong T., 1994, A&A 282, 127  
 Groenewegen M.A.T., Ludwig H.-G., 1998, A&A, accepted  
 Groenewegen M.A.T., Whitelock P.A., 1996, MNRAS 281, 1347  
 Groenewegen M.A.T., Baas F., de Jong T., Loup C., 1996, A&A 306, 241  
 Groenewegen M.A.T., van der Veen W.E.C.J., Lefloch B., Omont A., 1997, A&A 322, L21  
 Groenewegen M.A.T., Whitelock P.A., Smith C.H., Kerschbaum F., 1998, MNRAS 293, 18  
 Habing H.J., Tignon J., Tielens A.G.G.M., 1994, A&A 286, 523  
 Hills, R., 1996, The JCMT Newsletter 6, 32  
 Huggins P.J., Olofsson H., Johansson L.E.B., 1988, ApJ 332, 1009  
 Ivezić Z., Elitzur M., 1995, ApJ 445, 415  
 Ivezić Z., Elitzur M., 1996, MNRAS 279, 1011  
 Kahane C., Cernicharo J., Gomez-Gonzalez J., Guélin M., 1992, A&A 256, 235  
 Kastner J.H., 1992, ApJ 401, 337  
 Knapp G.R., Morris M., 1985, ApJ 292, 640  
 Knapp G.R., Chang K.M., 1985, ApJ 293, 281  
 Koepf G.A., Buhl D., Chin G., et al., 1982, ApJ 260, 584  
 Kwan J., Hill F., 1977, ApJ 215, 781  
 Kwan J., Linke R.A., 1982, ApJ 254, 587  
 Kwan J., Webster Z., 1993, ApJ 419, 674  
 Le Bertre T., 1992, A&AS 94, 377  
 Loup C., Forveille T., Omont A., Paul J.F., 1993, A&AS 99, 291  
 Mamon M., Glassgold A.E., Huggins P.J., 1988, ApJ 328, 797

- Morris M., Lucas R., Omont A., 1985, A&A 142, 107  
 Netzer N., Elitzur M., 1993, ApJ 410, 701  
 Olofsson H., Eriksson K., Gustafsson B., Carlström U., 1993, ApJS 87, 267  
 Sahai R., 1987, ApJ 318, 809  
 Stanek K.Z., Knapp G.R., Young K., Phillips T.G., 1995, ApJS 100, 169  
 Truong-Bach, Morris D., Nguyen-Q-Rieu, 1991, A&A 249, 435  
 Wang Y., Jaffe D.T., Graf U.U., Evans II N.J., 1994, ApJS 95, 503  
 Wannier P.G., Sahai R., 1986, ApJ 311, 335  
 Wannier P.G., Sahai R., Andersson B.-G., Johnson H.R., 1990, ApJ 358, 251  
 Wattenbach R., Krügel E., Röser H.P., et al., 1988, A&A 202, 133  
 Williams P.G., White G.J., 1992, A&A 266, 365  
 Winters J.M., Dominik C., Sedlmayer E., 1994a, A&A 288, 255  
 Winters J.M., Fleischer A.J., Gauger A., Sedlmayer E., 1994b, A&A 290, 623  
 Winters J.M., Fleischer A.J., Le Bertre T., Sedlmayer E., 1997a, A&A 326, 305  
 Winters J.M., Fleischer A.J., Sedlmayer E., 1997b, in: "Science with the VLT interferometer", Springer verlag, Berlin, p. 403